Inorganic Chemistry
Article

Inorg. Chem. **2010**, *49*, 3297–3304 **3297**
DOI: 10.1021/ic9022823

Interplay between the Crystalline and Magnetic Structures in Lightly Cr-Doped $Bi_{0.37}Ca_{0.63}Mn_{0.96}Cr_{0.04}O_{2.99}$

Chun-Chuen Yang,[†] Wen-Hsien Li,[*,‡] Chun-Ming Wu,[‡] Carissa H. C. Li,[‡] Jirong Sun,[§] and Jeffrey W. Lynn[∥]

[†]*Department of Physics, Chung-Yuan Christian University, Jhongli, 32023 Taiwan,* [‡]*Department of Physics and Center for Neutron Beam Applications, National Central University, Jhongli, 32001 Taiwan,* [§]*State Key Laboratory for magnetism, Institute of Physics and Center for Condensed Matter Physics, Chinese Academy of Science, Beijing, 10008 China, and* [∥]*NIST Center for Neutron Research, National Institute of Standards and Technology, Gaithersburg, Maryland 20899*

Received November 17, 2009

The interplay between the crystalline and magnetic structures of a 4% Cr-doped $Bi_{0.37}Ca_{0.63}Mn_{0.96}Cr_{0.04}O_{2.99}$ has been investigated by alternating current (ac) magnetic susceptibility, electrical resistivity, and neutron diffraction measurements. The compound crystallizes into a monoclinic $P2_1/m$ symmetry. A Jahn−Teller distortion occurs at 280 K. The thermal behavior of charge transport may be described by a three-dimensional variable range hopping conduction. Strong interplay between the localized magnetic electrons and the itinerant electrons are clearly revealed as the localization length increases by 20% when the Mn spins become ordered below 85 K. Short range magnetic correlations persist up to 160 K. The collinear magnetic structure can be viewed as consisting of ferromagnetic spin-trimers antiferromagnetically embedded in a ferromagnetic environment. Cr-doping reduces the charge ordering temperature and the magnetic ordering temperature. It nevertheless introduces long-range ferromagnetism.

Introduction

The strong interplay between the crystalline structure, electrical transport, and spin magnetism has generated a large variety of interesting properties[1−9] in hole-doped perovskite manganese oxides $(Ln_{1-x}A_x)(Mn_{1-y}B_y)O_3$, where *Ln* is a lanthanide ion, *A* is an alkaline-earth metal, and *B* is a transition metal. It is known that the physical properties of this class of materials are sensitive to A-site as well as B-site doping. Generally speaking, A-site doping creates a Mn^{3+}/Mn^{4+} mixed-valence state that not only affects the carrier density but also significantly influences the colossal magnetoresistance exhibited by this class of material.[9] B-site doping, on the other hand, disrupts the electrically and magnetically active Mn−O−Mn network, weakening the double exchange (DE) interaction, and is believed to be detrimental to the conduction mechanism.[10] Many studies have focused on the colossal magnetoresistive phenomena that appear in the charge ordered phase in mixed-valence compounds. Charge ordering (CO) is nowadays believed to be associated with the occurrence of the Jahn−Teller distortion,[11] which also results in a bending of the Mn^{3+}−O−Mn^{4+} DE path that in turn reduces the charge-spin coupling strength. The fundamental differences in the orbital symmetry of the $t_{2g}^3e_g^1$ and $t_{2g}^3e_g^0$ electronic configurations for Mn^{3+} and Mn^{4+} ions, respectively, are the crucial factors for the occurrence of Jahn−Teller distortion in mixed-valence compounds. A possible means for helping to reduce the distortion in MnO_6 octahedrons would be to incorporate into the compounds trivalent ions that have an identical electronic configuration to that of Mn^{4+}, such as Cr^{3+}. Recent studies have shown that Cr-doping can create a ferromagnetic microregion around each Cr^{3+} ion,[12] which in turn provides a magnetic environment that the DE interaction favors. However, the charge ordering temperature T_{CO} shifts to a lower temperature when Cr ions are incorporated onto the Mn sites.[8,13,14] A reduction of 8 K

*To whom correspondence should be addressed. E-mail: whli@phy.ncu.edu.tw.

(1) Zener, C. *Phys. Rev. B.* **1951**, *82*, 403.
(2) Anderson, P. W.; Hasegawa, H. *Phys. Rev.* **1955**, *100*, 675.
(3) de Gennes, P.-G. *Phys. Rev.* **1960**, *118*, 141.
(4) Goodenough, J. B. *Phys. Rev.* **1955**, *100*, 564.
(5) Wollan, E. O.; Koehler, W. C. *Phys. Rev.* **1955**, *100*, 545.
(6) Li, J. Q.; Uehara, M.; Tsuruta, C.; Matsui, Y.; Zhao, Z. X. *Phys. Rev. Lett.* **1999**, *82*, 2386.
(7) Wu, S. Y.; Li, W.-H.; Yang, C. C.; Lynn, J. W.; Liu, R. S. *Phys. Status Solidi B* **2007**, *244*, 2233.
(8) Lu, W. J.; Sun, Y. P.; Zhao, B. C.; Zhu, X. B.; Song, W. H. *Phys. Rev. B.* **2006**, *73*, 214409.
(9) Jin, S.; Tiefel, T. H.; McCormack, M.; Fastnacht, R. A.; Ramesh, R.; Chen, L. H. *Science* **1994**, *264*, 413.
(10) Ramesha, K.; Thangadurai, V.; Sutar, D.; Aubramanyam, S. V.; Subbanna, G. N.; Gopalakrishnan, J. *Mater. Res. Bull.* **2000**, *35*, 559.
(11) Radaelli, P. G.; Cox, D. E.; Marezio, M.; Cheong, S.-W. *Phys. Rev. B.* **1997**, *55*, 3015.
(12) Moritomo, Y.; Machida, A.; Mori, S.; Yamamoto, N.; Nakamura, A. *Phys. Rev. B.* **1999**, *60*, 9220.
(13) Martinelli, A.; Ferretti, M.; Castellano, C.; Mondelli, C.; Cimberle, M. R.; Tropeano, M.; Ritter, C. *Phys. Rev. B.* **2006**, *73*, 064423.
(14) Capogna, L.; Martinelli, A.; Francesconi, M. G.; Radaelli, P. G.; Rodriguez-Carvajal, J.; Cabeza, O.; Ferretti, M.; Castellano, C.; Corridoni, T.; Pompeo, N. *Phys. Rev. B* **2008**, *77*, 104438.

Published on Web 02/23/2010

in T_{CO} per 1% Cr-doping has been observed.[8] On the other hand, the Bi^{3+} ions have uniquely polarized $6s^2$ lone pairs and a noticeably smaller ionic size than that of Ln^{3+}, which frequently cause distortions in the crystalline structure.[15,16] Conductivity and T_{CO} have been found to be very sensitive to the Bi content in the compounds.[17−22] T_{CO} has been found[15] to be progressively increasing as more and more Bi ions are incorporated onto the lanthanide sites. The increase rate, however, is largely reduced once the Bi content exceeds 40%. Generally speaking, incorporation of Cr^{3+} ions onto the Mn sites helps create a ferromagnetic environment favored by the DE interaction, but disturb the stability of the charge order state that nevertheless can be compensated by introducing Bi onto the lanthanide sites. In this article, we report on the results of studies made on the magnetic and transport behaviors of a 4% Cr-doped $Bi_{0.37}Ca_{x0.53}Mn_{0.96}Cr_{0.04}O_{2.99}$. The interplay between the magnetic and conduction electrons is clearly revealed as the resistivity greatly increases when the Mn spins become ordered. Significant magnetic correlations of the Mn spins begin to develop below 160 K, and magnetic order develops below 85 K, with a spin arrangement consisting of ferromagnetic Mn trimers antiferromagnetically embedded in a ferromagnetic environment.

Experimental Section

A polycrystalline sample with a nominal composition of $Bi_{0.4}Ca_{0.6}Mn_{0.96}Cr_{0.04}O_3$ was synthesized using the conventional ceramic route. The stoichiometric precursor and well mixed powders of Bi_2O_3, CaO, Cr_2O_3, and $MnCO_3$ were first preheated at 900 °C in an air atmosphere for 24 h. The resultant powders were reground, pressed into pellets, and sintered at 1050 °C in a flowing-oxygen atmosphere for 36 h. The final products were then naturally cooled to room temperature. X-ray diffraction was used to first characterize the sample, pellet by pellet. No obvious differences were found in the X-ray diffraction patterns taken from different portions of the sample.

High-resolution neutron powder-diffraction was then employed to determine the detailed crystalline structure. The measurements were performed at the NIST Center for Neutron Research. The data were collected on BT-1, the 32-detector powder diffractometer, employing a Cu(311) monochromator crystal to extract neutrons of wavelength 1.5401 Å. Angular collimators, with horizontal divergences of 15′, 20′, and 7′ full width at half-maximum (fwhm) acceptance, were employed for the in-pile, monochromatic, and diffracted beams, respectively. For the measurement the sample was loaded into a cylindrical vanadium-can, which gives rise to no measurable neutron diffraction peaks. The diffraction patterns were analyzed using the General Structure Analysis System (GSAS) program[23] following the Rietveld refinement method.[24]

To search for the magnetic responses, the temperature profiles of the alternating current (ac) magnetic susceptibility were measured with and without the presence of an H_a. These measurements were performed with a Quantum Design "Physical Property Measurement System" employing the standard setup, where the sample was subjected to a weak driving ac magnetic field. The response of the system was then detected using two identical sensing coils connected in opposition. During the measurements, ~1 g of the sample was loaded into a non-magnetic cylindrical container. A pumped ^{4}He cryostat was used to cool the sample, and the lowest temperature achieved was 1.8 K.

High intensity neutron diffraction patterns, covering certain temperature regimes where the susceptibility shows anomalies, were also collected to search for magnetic correlations. These measurements were conducted on the BT-9 triple-axis spectrometer at the NIST Center for Neutron Research, employing pyrolytic graphite PG(002) monochromator crystals to select an incident wavelength of $\lambda = 2.359$ Å, PG filters to suppress higher-order wavelength contamination, and a PG(002) analyzer crystal to discriminate against inelastic scattering. Angular collimators, with horizontal divergences of 40′, 48′, and 48′ fwhm acceptance, were employed for the in-pile, monochromatic, and diffracted beams, respectively. During these measurements ~5 g of the sample was loaded into a cylindrical vanadium-can. The sample temperature was controlled using a He-gas closed-cycle refrigerator equipped with a high powered heater.

Results and Discussion

Crystalline Structure. Many studies have concluded that perovskite-type manganese oxides crystallize into an orthorhombic *Pbnm* symmetry.[1,18,25] It is nowadays known that the crystalline structure of the doped compounds is quite sensitive to the chemical composition of these compounds.[26] Breakdowns of the orthorhombic symmetry into a monoclinic[20,27−29] or a triclinic[15,16] one in doped compounds have been reported. A triclinic symmetry of space group $P2_1/m$ for a Bi-rich $Bi_{0.6}Ca_{0.4}MnO_3$ has been proposed.[15,16] In this study, attention has been paid to search the possible crystalline symmetries for the present compound. Two types of crystalline structures, one belonging to the monoclinic $P2_1/m$ symmetry and the other to the orthorhombic *Pbnm* symmetry, are found to fit the diffraction patterns well. Figure 1 shows the portions of the full observed (circles) and fitted (solid lines) diffraction patterns around the characteristic {110}, {200}, {222}, {312}, and {330} reflections for the two structures. Clearly, the fit obtained using $P2_1/m$ symmetry ($\chi^2 = 1.387$) is noticeably better than the one obtained using *Pbnm* ($\chi^2 = 6.533$). In particular, the *Pbnm* symmetry not only poorly describes the intensities of the

(15) Woo, H.; Tyson, T. A.; Croft, M.; Cheong, S.-W.; Woicik, J. C. *Phys. Rev. B.* **2001**, *63*, 134412.
(16) Sugawara, F.; Iida, S.; Syono, Y.; Akimoto, S. *J. Phys. Soc. Jpn.* **1968**, *25*, 1553.
(17) Xiong, C. M.; Sun, J. R.; Li, R. W.; Zhang, S. Y.; Zhao, T. Y.; Shen, B. G. *J. Appl. Phys.* **2004**, *95*, 1336.
(18) Santhosh, P. N.; Goldberger, J.; Woodward, P. M.; Vogt, T.; Lee, W. P.; Epstein, A. J. *Phys. Rev. B.* **2000**, *62*, 14928.
(19) Chiba, H.; Kikuchi, M.; Kusaba, K.; Muraoka, Y.; Syono, Y. *Solid State Commun.* **1996**, *99*, 499.
(20) Bao, W.; Axe, J. D.; Chen, C. H.; Cheong, S.-W. *Phys. Rev. Lett.* **1997**, *78*, 543.
(21) Liu, H. L.; Cooper, S. L.; Cheong, S.-W. *Phys. Rev. Lett.* **1998**, *81*, 4684.
(22) García-Muñoz, J. L.; Frontera, C.; Aranda, M. A. G.; Llobet, A.; Ritter, C. *Phys. Rev. B.* **2001**, *63*, 064415.
(23) Larson, A. C.; Von Dreele, R. B. *General Structure Analysis System*, Report LA-UR-86-748; Los Alamos National Laboratory: Los Alamos, NM. 1990.
(24) Rietveld, H. M. *J. Appl. Crystallogr.* **1969**, *2*, 65.
(25) Huang, Q.; Santoro, A.; Lynn, J. W.; Erwin, R. W.; Borchers, J. A.; Peng, J. L.; Ghosh, K.; Greene, R. L. *Phys. Rev. B.* **1998**, *58*, 2684.
(26) For example see: *Colossal Magnetoresistance, Charge Ordering and Related Properties of Manganess Oxides*; Rao, C. N. R., Raveau, B., Eds.; World Scientific: Singapore, 1998.
(27) Wu, S. Y.; Yang, C. C.; Tsao, F. C.; Li, W.-H.; Lee, K. C.; Lynn, J. W.; Yang, H. D. *J. Phys.: Condens. Matter* **2002**, *14*, 12585.
(28) Hervieu, M.; Tendeloo, G. V.; Caignaert, V.; Maignan, A.; Raveau, B. *Phys. Rev. B.* **1996**, *53*, 14274.
(29) Lebedev, O. I.; Tendeloo, G. V.; Amelinckx, S.; Leibold, B.; Habermeier, H.-U. *Phys. Rev. B.* **1998**, *58*, 8065.

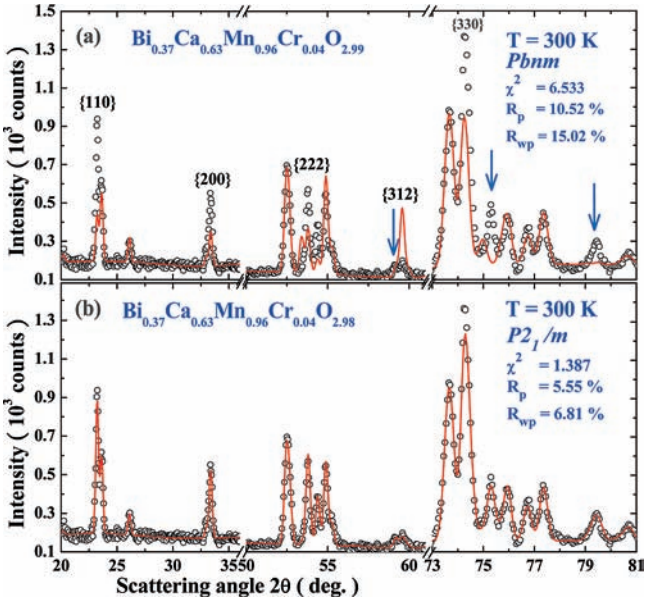

Figure 1. Portions of the observed (circles) and fitted (solid lines) high-resolution neutron powder-diffraction patterns around the characteristic {110}, {222}, and {330} reflections taken at 300 K, assuming (a) an orthorhombic *Pbnm* symmetry and (b) a monoclinic $P2_1/m$ symmetry. The fit using $P2_1/m$ symmetry is noticeably better than the one using *Pbnm*. The reflections at $2\theta = 75.30°$ and 79.45° cannot be accounted for when employing the *Pbnm* symmetry.

{110}, {200}, {222}, {312}, and {330} reflections but also misses the reflections at $2\theta = 59.1°$, 75.3, and 79.4°, as indicated by the arrows in Figure 1(a).

The full observed (crosses) and fitted (solid lines) diffraction patterns, assuming a monoclinic $P2_1/m$ crystalline symmetry, are displayed in Figure 2. A similar crystalline structure has also been observed in $La_{0.5}Ca_{0.5}MnO_3$ and $Pr_{0.7}Ca_{0.3}MnO_3$.[12,30] Analysis of the occupancy factors shows that all sites are fully occupied, except that the oxygen content is slightly deficient. The chemical composition obtained from the fit is $Bi_{0.37}Ca_{0.63}Mn_{0.964}Cr_{0.036}O_{2.99}$, which agrees very well with the nominal stoichiometric composition. The refined structural parameters are summarized in Table 1. No traces of impurity phases, such as Cr_2O_3 and $MnCO_3$, could be identified. We estimate the impurity phases in the sample to be less than 1%. No structural change is detected as the temperature is reduced from 300 to 30 K, the lowest temperature achieved in this study.

The monoclinic $P2_1/m$ structure can be viewed as a slightly distorted ($\beta = 89.864°$) orthorhombic *Pbnm* structure, leading to three different forms of MnO_6 octahedra and the crystalline unit cell doubled along the shortest crystallographic direction. There are three crystallographically inequivalent Mn sites in the unit cell, marked Mn(1), Mn(2), and Mn(3) for those located at the 2*a*, 2*b*, and 4*f* sites, respectively, as indicated in Table 1. Each site experiences a unique atomic environment. In particular, 62% of the doped Cr enters the 2*a* sites, while 20% and 18% enter the 2*b* and 4*f* sites, respectively.

Charge Ordering and Charge Segregation. The Jahn−Teller distortion is a well-known fundamental phenomenon

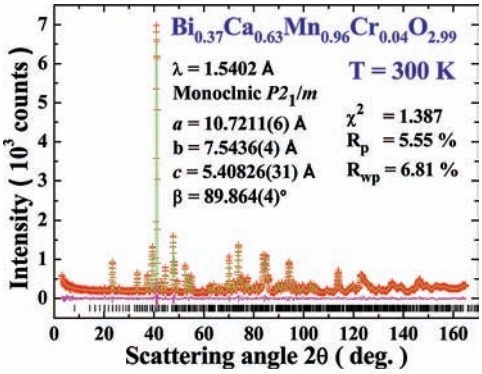

Figure 2. Observed (crosses) and fitted (solid lines) high-resolution neutron powder-diffraction patterns, assuming a monoclinic symmetry of space group $P2_1/m$. The difference between the calculated and observed is plotted at the bottom. The solid vertical lines mark the calculated positions of Bragg reflections for the proposed crystalline structure.

that occurs in perovskite manganese oxides. It can most often be recognized by the appearance of inflections in the thermal variation rates of the lattice parameters. Figure 3 shows the temperature dependencies of the lattice parameters. Inflection points at around 280 K are clearly revealed in all three lattice parameters, reflecting the occurrence of a structural phase transition that is likely originating from a Jahn−Teller distortion. On warming from 250 to 350 K through this transition, the axial lattice parameter *b* elongates by ~0.66% while the planar lattice parameters *a* and *c* shrink by ~0.28%. As a consequence the MnO_6 octahedra become thinner and taller at high temperatures, which is indeed the signature of a Jahn−Teller distortion.

It is known that the bond lengths between a Mn ion and its neighboring O ions are closely related to the valence of the Mn ion.[31] Thermal variations of the average Mn−O bond lengths for the three distinctive Mn sites are plotted in Figure 4, where the arrows indicate the expected average Mn^{3+}−O and Mn^{4+}−O bond lengths at low temperatures.[32,33] At low temperatures, the average bond lengths of the Mn ions at the 2*a* sites (marked ⟨Mn(1)−O⟩) and at the 2*b* sites (marked ⟨Mn(2)−O⟩) are ⟨Mn^{3+}−O⟩-like, whereas those at the 4*f* sites (marked ⟨Mn(3)−O⟩) are ⟨Mn^{4+}−O⟩-like. Similar results have also been reported[11,30,34] for Cr-free compounds. Taking that the Mn ions at the 2*a*/2*b* and 4*f* sites are trivalent and tetravalent, respectively, the average valence for Mn ions is then +3.48, which agrees well with the value of +3.50 derived from the refined stoichiometric composition of $Bi_{0.37}Ca_{0.63}Mn_{0.964}Cr_{0.036}O_{2.99}$. Accordingly, alternative Mn^{3+}−Mn^{4+} charge planes are formed at low temperatures. The charge distribution may then be viewed as consisting of Mn^{3+}(2*a*)−Mn^{4+}(4*f*)−Mn^{3+}(2*b*)−Mn^{4+}(4*f*) charge planes, when viewed along the *c* crystallographic direction. These charge planes gradually melt at higher temperatures. Above 100 K, the valences at the three Mn sites become

(30) Cox, D. E.; Radaelli, P. G.; Marezio, M.; Cheong, S.-W. *Phys. Rev. B.* **1998**, *57*, 3305.

(31) Brese, N. E.; O'Keeffe, M. *Acta Crystallogr., Sect. B.* **1991**, *47*, 192.

(32) Grant, R. W.; Geller, S.; Cape, J. A.; Espinosa, G. P. *Phys. Rev.* **1968**, *175*, 686.

(33) Baur, W. H. *Acta. Crystallogr. B* **1976**, *32*, 2200. Kirchner, H. P. *J. Am. Ceram. Soc.* **1969**, *52*, 379. Hazony, Y.; Parkins, H. K. *J. Appl. Phys.* **1970**, *41*, 5130.

(34) Gontchar, E.; Nikiforov, A. E.; Popov, S. E. *J. Magn. Magn. Mater.* **2001**, *223*, 175.

Table 1. List of the Refined Structural Parameters of $Bi_{0.37}Ca_{0.63}Mn_{0.964}Cr_{0.036}O_{2.99}$ at 300 K, Where B_{iso} Represents the Isotropic Temperature Parameter and M Represents the Multiplicity

$Bi_{0.37}Ca_{0.63}Mn_{0.964}Cr_{0.036}O_{2.99}$ at 300 K[a]						
	x	y	z	M	B_{iso}(Å^2)	occupancy
Bi/Ca(1)	0.2570(11)	1/4	−0.0407(21)	2*e*	0.98(19)	0.46(4)/0.54(4)
Bi/Ca(2)	0.5017(12)	3/4	0.5378(24)	2*e*	0.23(21)	0.47(5)/0.53(5)
Bi/Ca(3)	0.7557(14)	1/4	−0.0312(26)	2*e*	0.74(24)	0.29(5)/0.71(5)
Bi/Ca(4)	0.9994(13)	3/4	0.5434(25)	2*e*	1.50(21)	0.27(4)/0.73(4)
Mn/Cr(1)	0	0	0	2*a*	2.57(58)	0.90(2)/0.10(2)
Mn/Cr(2)	1/2	0	0	2*b*	0.08(21)	0.97(2)/0.03(2)
Mn/Cr(3)	0.2533(16)	0.0092(19)	0.5159(25)	4*f*	0.47(18)	0.99(2)/0.01(2)
O(1)	0.5345(11)	1/4	0.0200(21)	2*e*	0.77(28)	1.00(6)
O(2)	0.2838(10)	3/4	0.4722(21)	2*e*	0.43(24)	0.91(5)
O(3)	1.0410(18)	1/4	0.0193(35)	2*e*	2.80(51)	1.00(7)
O(4)	0.7846(11)	3/4	0.5063(20)	2*e*	0.45(27)	0.99(5)
O(5)	0.3939(9)	0.0334(13)	0.7053(16)	4*f*	0.53(24)	1.00(4)
O(6)	0.3585(9)	1.0365(17)	0.2099(20)	4*f*	1.18(28)	0.96(4)
O(7)	0.1054(8)	0.9543(12)	0.2740(15)	4*f*	1.05(19)	1.00(4)
O(8)	0.1455(8)	−0.0321(14)	0.7878(17)	4*f*	1.01(25)	0.99(4)

[a] Monoclinic $P2_1/m$ (No. 11). a = 10.7211(6) Å, b = 7.5436(4) Å, c = 5.4083(3) Å, β = 89.864(4)°. χ^2 = 1.387, R_p = 5.55%, R_{wp} = 6.81%.

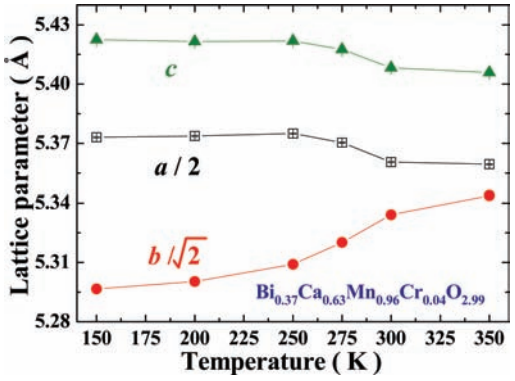

Figure 3. Temperature dependence of the lattice parameters. Anomalies are clearly revealed at around 280 K in all three curves, reflecting the occurrence of the Jahn−Teller distortion. On warming from 250 to 350 K, the axial lattice parameter b elongates by ∼0.66% while the planar lattice parameters a and c shrink by ∼0.28%,.

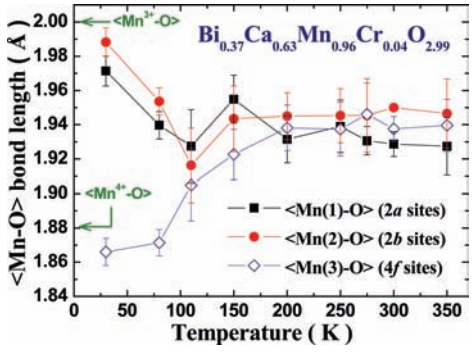

Figure 4. Thermal variations in the average Mn−O bond lengths at the three distinctive Mn sites. The arrows indicate the expected average Mn^{3+}−O and Mn^{4+}−O bond lengths at low temperatures.

indistinguishable, as can be seen in Figure 4. An average valence of +3.50 may then be expected at each Mn site. This result agrees with the assumption that alternative Mn^{3+} and Mn^{4+} zigzag chains form in the charge order state, as proposed by Goodenough.[4]

Hopping Conduction. The thermal variations of the electrical resistivity $\rho(T)$ measured at various applied magnetic fields H_a are illustrated in Figure 5. These resistivity data are taken employing the standard four-probe setup, operated in the constant current mode. The main features observed are the resistivity drops by a factor of ∼10^7 upon warming from 45 to 300 K, an abrupt change in the thermal reduction rate of ρ that appears at around 280 K, and there is a large change in the magnetic reduction rate of ρ when H_a exceeds 6 T. The resistivity decreases by ∼2% and ∼20% per tesla when H_a is smaller and greater than 6 T, respectively. This indicates that the localized charges can be effectively released by an H_a that is greater than 6 T. The inflection at 280 K echoes the occurrence of the Jahn−Teller distortion. Charge ordering often accompanies the Jahn−Teller distortion.[11] A linear dependence of the charge ordering temperature T_{CO} on the tolerance factor t and on the Cr composition y has been reported[8,17,22,35] for Cr-doped compounds. T_{CO} of Bi-based and Cr-doped compounds can then be estimated by scaling the $T_{CO}(t)$ plot shown in Figure 3 of ref 22 together with the $T_{CO}(y)$ plot shown in Figure 6 of ref 17. Accordingly, T_{CO} = 3494 − 3408t − 1729y with t = 0.921 and y = 0.04 gives an expected T_{CO} = 286 K for

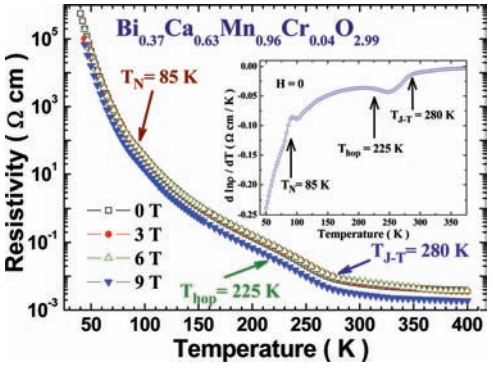

Figure 5. Temperature dependence of the resistivity taken at various applied magnetic fields. Significant reductions in the resistivities are seen when H_a exceeds 6 T. The inset shows the thermal variations of d(ln ρ)/dT, where an inflection is clearly revealed at 85 K.

(35) Woodward, M.; Vogt, T.; Cox, D. E.; Arulraj, A.; Rao, C. N. R.; Karen, P.; Cheetham, A. K. *Chem. Mater.* **1999**, *10*, 3652.

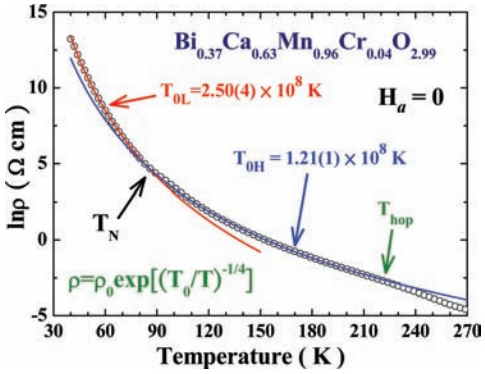

Figure 6. Fit (solid lines) of the observed (circles) $\rho(T)$ at $H_a = 0$ for a two-section 3D VRH conduction. The activation temperature increases by a factor of 2.1 when Mn spins become ordered below 85 K, which corresponds to a 20% increase in the localization length.

Table 2. Fitted Values for Effective Magnetic Moments, Curie Temperatures, and Activation Temperatures at Various Applied Magnetic Fields

	$T < T_N$	$T_N < T < T_{hop}$			$T > T_{hop}$	
$H(T)$	T_{0L} (10^8 K)	μ_{eff1} (μ_B)	$T_{\theta 1}$(K)	T_{0H} (10^8 K)	μ_{eff2} (μ_B)	$T_{\theta 2}$ (K)
0	2.63(1)	5.8(1)	−107(1)	1.21(1)	4.6(2)	141(6)
3	2.47(2)	5.8(2)	−111(2)	1.18(2)	4.6(2)	138(8)
6	2.45(2)			1.16(2)		
9	2.42(2)	6.0(2)	−129(1)	1.14(1)	4.6(2)	144(9)

the present compound, in excellent agreement with the 280 K observed for the present composition.

It is known that the electrical conduction in perovskite manganese oxides originates mainly from the thermally activated hopping of charge carriers. The $\rho(T)$ shown in Figure 6 may be described by assuming three-dimensional (3D) variable range hopping (VRH) conduction. This type of conduction is known[36] to vary with temperature as $\rho = \rho_0 \exp[(T_0/T)^{1/4}]$, where ρ_0 is a constant that indicates the base resistivity at high temperatures, $T_0 \equiv 24/[\pi N(E_F)\xi^3]$ is the activation temperature, $N(E_F)$ represents the density of states at the Fermi level, and ξ is the localization length. Close examination of $\rho(T)$ reveals a small but noticeable change in the thermal variation rate of ρ at around 85 K, as can be seen in the $d(\ln \rho)/dT$ plot shown in the inset to Figure 5. Note that below 85 K long-range ordering of the Mn spins develops (see below). The increase in the thermal variation rate of ρ as the Mn spins become ordered signals the existence of noticeable spin-charge couplings in the present compound. Figure 6 shows the $\rho(T)$ curve, taken at $H_a = 0$, together with the fit (solid curves) for a two-section 3D VRH conduction, where T_{0L} and T_{0H} mark the activation temperatures below and above 85 K, respectively. The fitted values for T_{0L} and T_{0H} are listed in Table 2. Accordingly, the activation temperature increases by a factor of 2.1 once the Mn spins become ordered, which corresponds to a 20% increase in the localization length. In addition, both T_{0L} and T_{0H} gradually decrease with increasing H_a, indicating that the hopping barrier is reduced or the localized charges become partially melted by the application of a magnetic field. Another change in ξ occurs at

(36) For example, see: Isihara, A. *Condensed Matter Physics*; Oxford Univ. Press: New York, 1991; p 157.

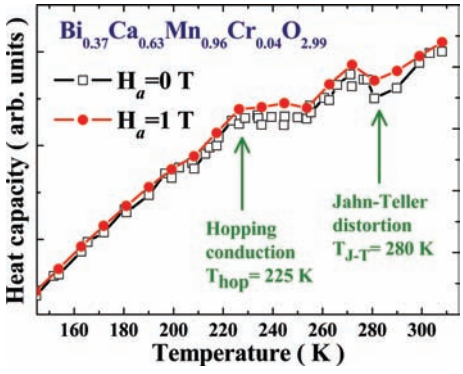

Figure 7. Temperature dependence of the specific heat taken at $H_a = 0$ and 1 T, revealing two anomalies at 225 and 280 K. There is a small increase in the in-field specific heat.

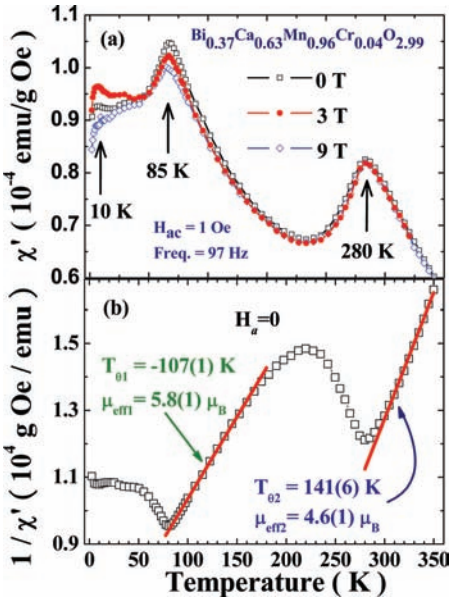

Figure 8. Temperature dependence of (a) the in-phase component χ' of the ac magnetic susceptibility and (b) $1/\chi'$ using a probing field with a rms strength of 1 Oe and a frequency of 97 Hz. Three anomalies at 280, 85, and 10 K are clearly revealed.

~225 K, above which we have no direct experimental evidence to conclude whether 3D VRH remains to be the main mechanism for charge transport. This inflection at 225 K is also revealed in the temperature profiles of the specific heat, as shown in Figure 7, where the inflection associated with the Jahn−Teller distortion is also clearly seen at 280 K. A small increase may be identified between the specific heat data taken with $H_a = 1$ T compared with the data obtained at $H_a = 0$ T.

Magnetic Responses. The temperature profiles of the in-phase component χ' of the ac magnetic susceptibility taken at various H_a are shown in Figure 8a. These data were taken using a weak probing field with a root-mean-square strength of 1 Oe and a frequency of 97 Hz. There are three clear anomalies (at 280, 85, and 10 K) revealed in the $\chi'(T)$ curves. The presence of an H_a up to 9 T results in no noticeable shifts in the peak positions in $\chi'(T)$ but slightly reduces the magnitudes of the two peaks at low temperatures. Non-zero values for χ' are obtained at low temperatures together with H_a resulting in a reduction in the magnitudes of the peak at 85 K, signaling the

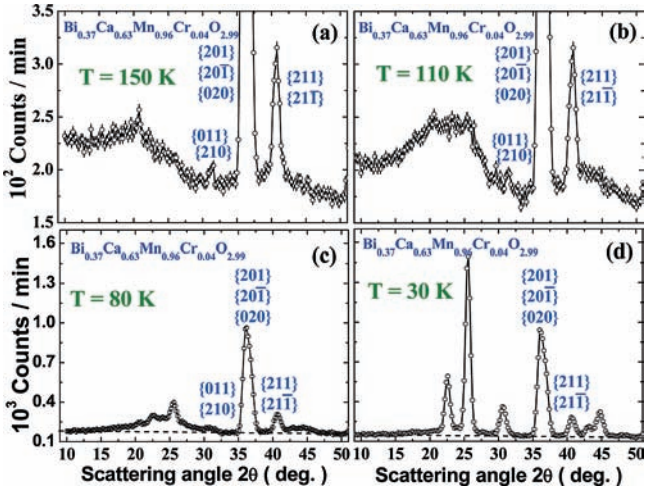

Figure 9. High intensity neuron diffraction patterns taken at four representative temperatures. In addition to the unclear {011}+{210}, {201}+{020} and {211} reflections, correlated magnetic intensities are already evident at 150 K. At 30 K, the magnetic Bragg peaks are resolution limited, indicating long-range magnetic order of the Mn ions.

appearance of both ferromagnetic and antiferromagnetic components when Mn spins become ordered. The Curie−Weiss behavior expected for the paramagnetic state is unfortunately altered by the appearance of the peak associated with the Jahn−Teller distortion at 280 K. Nevertheless, the portions where the Curie−Weiss behavior remains unaltered may be revealed in the $1/\chi'(T)$ plot shown in Figure 8b. Two straight sections that signify Curie−Weiss behavior (solid lines) are revealed. Interestingly, the effective moments obtained for the two temperature sections are substantially different, with the low temperature one μ_{eff1} being 26% larger than the high temperature one μ_{eff2}, as listed in the plot. More importantly, the value of $\mu_{\text{eff1}} = 5.8\,\mu_B$ substantially exceeds the 4.4 μ_B expected for free $Mn^{3.5+}$ ions, indicating that magnetic correlations exist above 85 K. This remarkable characteristic of exceedingly large effective moments observed in half-doped manganites is nowadays understood as the ordering of 4-fold Mn units, known as Zener polarons,[37−39] above the Neel temperature. These magnetic correlations diminish upon warming and eventually disappear at higher temperatures.

Magnetic Correlations. Figure 9 displays the neutron diffraction patterns taken at four representative temperatures. In addition to the nuclear {011}+{210}, {201}+{020} and {211} reflections, there are extra broad peaks clearly revealed at 150 K, as can be seen in Figure 9(a). This temperature is well above the ordering temperature of 85 K for the Mn spins, as indicated by the magnetic susceptibility data (Figure 8) and the order parameter measurements (see below). The magnetic scattering appears as broad peaks in the diffraction pattern, signaling the development of short-range magnetic correlations among the Mn spins. The magnetic correlation length reaches ~100 Å at 110 K. Apparently, it is the short-range

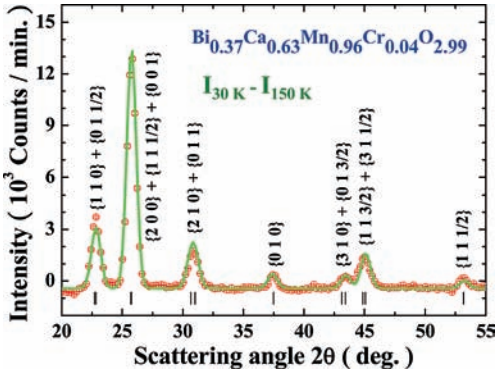

Figure 10. Neuron magnetic diffraction pattern obtained at 30 K, where the indices shown are based on the nuclear unit cell. The solid lines indicate the calculated pattern based on the proposed magnetic structure, using a Gaussian resolution function with $\langle \mu_Z \rangle_{Mn}{}^{3+} = 3.62(3)\,\mu_B$ and $\langle \mu_Z \rangle_{Mn}{}^{4+} = 2.87(4)\,\mu_B$.

magnetic correlations which appear above the ordering temperature that give rise to an effective moment 26% higher than what is expected from free $Mn^{3.5+}$ ions.

The magnetic intensities evolve into resolution limited peaks at 30 K, as shown in Figure 9d, indicating that long-range Mn spin ordering has developed. To isolate the magnetic signal from the nuclear ones, the diffraction pattern taken at 150 K that serves as the non-magnetic background is then subtracted from the one taken at 30 K. This technique is applicable in cases where no structural change occurs within the temperature regime. Figure 10 shows the difference pattern between 30 and 150 K, where seven resolution limited peaks are clearly revealed and the indices shown are based on the nuclear unit cell. This pattern may be used to determine the spin arrangement of the Mn ions. The appearance of half-integers for the Miller's indices of the *a* and *c* crystallographic directions showing that the magnetic unit cell is double the nuclear one along these two crystallographic directions. Many possible models for the spin configuration were considered. In particular, a spin arrangement consists of antiferromagnetically coupled ferromagnetic chains, or ferromagnetically coupled antiferromagnetic chains, or antiferromagnetically coupled ferromagnetic planes fits poorly to the observed pattern. The spin arrangement that fits the observed pattern reasonably well is plotted in Figure 11. Accordingly, the Mn spins on the 2*a* sites are ferromagnetically aligned; those on the 2*b* sites are antiferromagnetically aligned; while those on the 4*f* sites are antiferromagnetically aligned along the basal *c*-axis direction and ferromagnetically aligned along the axial *b*-axis direction. Structural analysis has shown that the Cr dopant has a preference to enter the 2*a* site (62% of them). The long-range ferromagnetism of the Mn spins on the 2*a* sites can be a direct result of the appearance of Cr ions on these sites. Previous studies[12,17,40,41] have demonstrated that Cr-doping reduces the charge ordering temperature and the magnetic ordering temperature, the present results further signal that it nevertheless introduces long-range ferromagnetism and echoes Cr-doping

(37) Zhou, J.-S.; Goodemough, J. *Phys. Rev. B* **2000**, *62*, 3834.
(38) Daoud-Aladine, A.; Rodriguez-Carvajal, J.; Pinsard-Gaudart, L.; Fernandez-Diaz, M. T.; Revcolevschi, A. *Phys. Rev. Lett.* **2002**, *89*, 097205–1.
(39) Daoud-Aladine, A.; Perca, C.; Pinsard-Gaudart, L.; Rodriguez-Carvajal, J. *Phys. Rev. Lett.* **2008**, *101*, 166404–1.
(40) Raveau, B.; Maignan, A.; Martin, C. *J. Solid State Chem.* **1997**, *130*, 162.
(41) Damay, F.; Martin, C.; Maignan, A.; Hervieu, M.; Raveau, B.; Bouree, F.; Andre, G. *Appl. Phys. Lett.* **1998**, *73*, 3772.

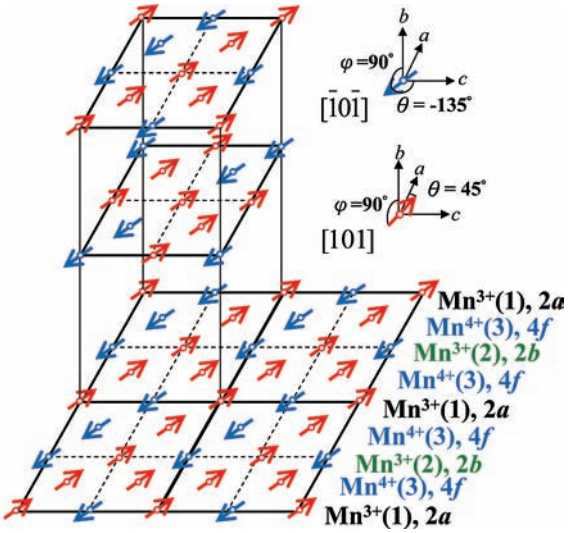

Figure 11. Proposed magnetic structure of the Mn ions. This collinear spin arrangement consists of ferromagnetic spin-trimers (along the [10$\bar{1}$] crystallographic direction) antiferromagnetically embedded in a ferromagnetic environment, with the moments pointing in the [101] direction.

can[12] create ferromagnetic microregion around each Cr^{3+} ions. This proposed collinear spin arrangement can also be viewed as consists of ferromagnetic spin-trimers (along the [$\bar{1}$0$\bar{1}$] crystallographic direction) antiferromagnetically embedded in a ferromagnetic environment. However, only 3/8 of the Mn ions form spin-trimers. The solid curve in Figure 10 indicates the calculated diffraction pattern based on the proposed magnetic structure, with $\langle\mu_Z\rangle_{Mn}{}^{3+} = 3.62(3)\ \mu_B$ and $\langle\mu_Z\rangle_{Mn}{}^{4+} = 2.87(4)\ \mu_B$. The calculated pattern agrees reasonably well with the observed one. We remark that magnetic phase segregation has been found[41−43] in several Mn substituted half doped manganites. However, no sign of the presence of a second magnetic phase can be identified from the present data. One possible situation is that they cannot be resolved from the present data. Nevertheless, the proposed magnetic phase still reveals the main phase even if a second phase does exist.

The formation of the proposed magnetic structure may be understood by examining the magnetic interactions between the Mn ions. It is the O-mediated superexchange (SE) interaction that governs the magnetic interactions between two Mn ions in the present compound. The SE integrals J of these interactions can readily be calculated by Gontchar's method[44] and the Bloch dependency[34,45] $J \sim \cos^2\varphi/r^{10}$, where φ is the Mn−O−Mn bond angle and r is the Mn−O bond length. Although the sign of the SE integral depends on the occupied e_g orbits (Goodenough−Kanamory−Anderson rule), the strength of the interaction can still be calculated without knowing the status of the occupied orbits. There are eight nearest neighbor Mn−O−Mn SE paths that may be indentified for each Mn ion. Among them, two Mn(3)−O−Mn(1) and two

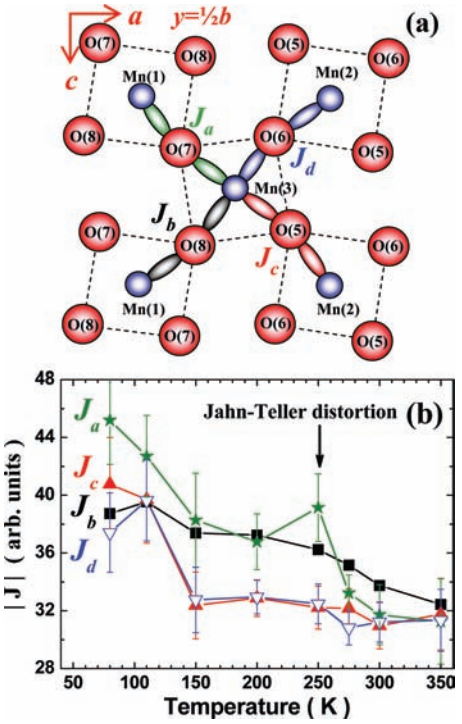

Figure 12. (a) Schematic drawing of the four in-plane Mn−O−Mn SE paths. (b) Temperature dependence of the absolute values of the exchange integrals of the four in-plane SE interactions. The strengths of all four SE interactions noticeably increase below 150 K.

Mn(3)−O−Mn(2) paths lie in the *a*-*c* plane, as illustrated in Figure 12(a). Figure 12(b) shows the temperature dependencies of the absolute values of the SE integrals $|J_a|$, $|J_b|$, $|J_c|$, and $|J_d|$ of the Mn(3)−O(6)−Mn(1), Mn(3)−O(8)−Mn(1), Mn(3)−O(5)−Mn(2), and Mn(3)−O(6)−Mn(2) paths, respectively. The other four Mn−O−Mn paths point in the [010] direction, as illustrated in Figure 13(a). Of these the two Mn(3)−O−Mn(3) paths are identical. Figure 13(b) shows the temperature dependencies of the absolute values of the SE integrals $|J_e|$, $|J_f|$, and $|J_g|$ of the Mn(1)−O(3)−Mn(1), Mn(2)−O(3)−Mn(2), and Mn(3)−O(2)−Mn(3) paths, respectively. The results show that the strengths of all eight SE interactions increase noticeably below 150 K, echoing the development of magnetic correlations among the Mn spins. The intraplane exchange integrals (J_a, J_b, J_c, and J_d) are ∼1.5 times stronger than the interplane ones (J_e, J_f, and J_g), favoring a magnetic structure with the ordered moments that lie in the *a*-*c* planes. In addition, the couplings along the [101] direction (J_a and J_c) are considerably larger than those along the [10$\bar{1}$] direction (J_b and J_d). Note that the Jahn−Teller distortion results in different degrees of modification in the SE coupling strengths along each path, as can be seen in Figures 12b and 13b.

The temperature dependencies of the peak intensities at the {210}+{011} and at the {200}+{111/2}+{001} positions are plotted in Figure 14. This plot shows the variations of the square of the magnetization with temperature, and reveals the typical order-parameter curves of a polycrystalline sample. No noticeable differences may be identified between the temperature profiles of the two curves, which indicate that the ferromagnetic and

(42) Yaicle, C.; Martin, C.; Jirak, Z.; Fauth, F.; Andre, G.; Suard, E.; Maignan, A.; Hardy, V.; Retoux, R.; Hervieu, M.; Hebert, S.; Raveau, B.; Simon, Ch.; Saurel, D.; Brulet, A.; Bouree, F. *Phys. Rev. B* **2003**, *68*, 224412.
(43) Yaicle, C.; Frontera, C.; Garcia-Munoz, J. L.; Martin, C.; Maignan, A.; Andre, G.; Bouree, F.; Ritter, C.; Margiolaki, I. *Phys. Rev. B* **2006**, *74*, 144406.
(44) Gontchar, L. E.; Nikiforov, A. E. *Phys. Rev. B.* **2002**, *66*, 014437.
(45) Kanamori, J. *J. Appl. Phys.* **1960**, *31*, 14S.

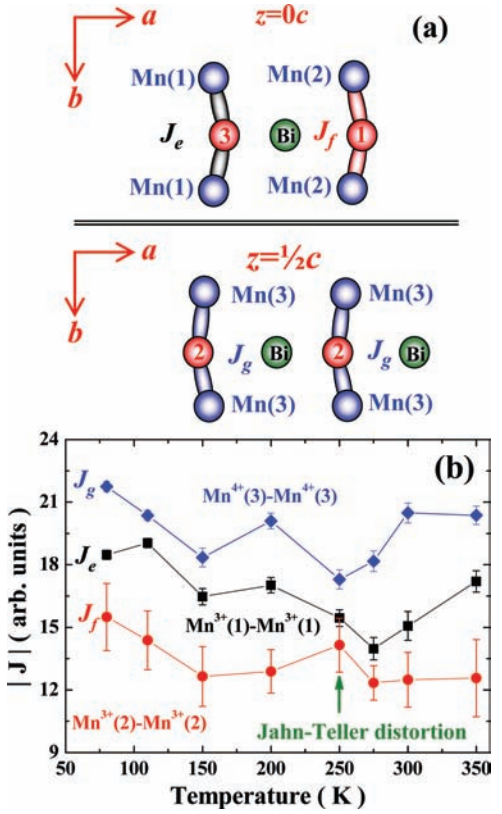

Figure 13. (a) Schematic drawing of the three axial Mn−O−Mn SE paths. Among them the two Mn(3)−O−Mn(3) paths are identical. (b) Temperature dependence of the absolute values of the exchange integrals of the three axial SE interactions. The strengths of all three SE interactions noticeably increase below 150 K.

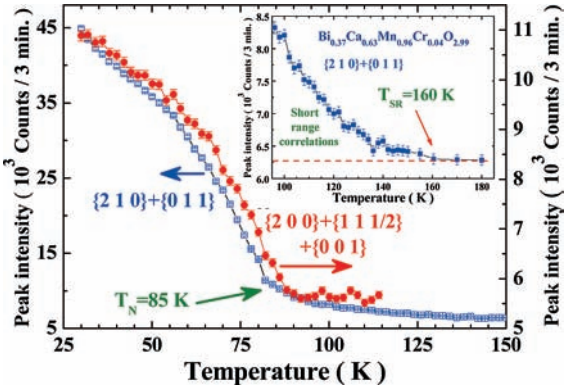

Figure 14. Temperature profiles of the peak intensities at the {210}+{011} and {200}+{111/2}+{001} positions, showing a $T_N \approx 85$ K for the Mn spins. The inset shows the magnetic intensities observed above T_N, where the dashed line indicates the background intensity.

antiferromagnetic components develop simultaneously, and they act as a whole. The ordering temperature of the Mn spins, as determined by the inflection point of the order parameter curves, is $T_N \approx 85$ K, which matches the temperature at which $\chi'(T)$ shows an anomaly. Interestingly, the T_N of the 4% Cr-doped compound is significantly lower than the value of $T_N \approx 140$ K reported[17] for the undoped compound. However, the magnetic intensities, and hence the magnetic correlations, of the present Cr-doped compound appear at temperatures that are considerably higher than T_N, as can be seen in the inset to Figure 14, where the dashed line indicates the background intensity. Apparently, significant short-range magnetic correlations persist up to $T_{SR} \approx 160$ K. This T_{SR} obtained from neutron diffraction intensity agrees with the coupling strength calculations shown in Figures 12b and 13b, revealing that the SE coupling strengths increase noticeably below 150 K. This behavior may be understood as due to the replacement of Mn ions by Cr ions, which effectively interrupts the Mn−O−Mn SE paths, thereby weakening the long-range correlations but forming correlated clusters. Surprisingly, 4% Cr-doping results in such significant changes in the magnetic correlations.

Conclusions

Significant alternations in the magnetic and transport behaviors have been found when a small amount of Cr ions is incorporated into the Mn sites of a Bi/Ca-based perovskite manganese oxide. The 4% Cr-doped $Bi_{0.37}Ca_{x0.53}Mn_{0.96}Cr_{0.04}O_{2.99}$ crystallizes into a monoclinic $P2_1/m$ symmetry. A Jahn−Teller distortion occurs at a significantly lower temperature of 280 K, compared to the 310 K reported for the Cr-free compound. Alternative Mn^{3+}−Mn^{4+} charge planes are formed below 100 K. The thermal behavior of the charge transport may be described by a three-dimensional variable range hopping conduction. Strong interplay between the localized magnetic electrons and the itinerant electrons are seen, as the localization length increases by 20% when the Mn spins become ordered. The ordering temperature of the Mn spins shifts to 85 K, which is significantly lower than the value of 140 K reported for the Cr-freed compound. However, short-range magnetic correlations persist up to 160 K. Exchange integral calculations favor a magnetic structure with moments that lie in the *a-c* plane and point in the [101] direction, which matches well with the magnetic structure proposed based on the neutron magnetic diffraction patterns. Most importantly, Cr-doping introduces long-range ferromagnetism, while reducing the magnetic ordering temperature.

Acknowledgment. Identification of commercial equipment in the text is not intended to imply recommendation or endorsement of said equipments by the National Institute of Standards and Technology. This work is supported by a grant from the National Science Council of Taiwan, under Grant NSC 98-2112-M-008-016-MY3 and the National Basic Research of China, under Grant 2007CB925002.